Supplementary Material

Highly stable photovoltaic effects in A^{2+}-Zr^{4+} (A=Ca, Sr, Ba) co-doped $BiFeO_3$ films with self-polarization

Lei Shi, Wenyue Zhao, Zhao Wang, Wenjing Hua, Xiaoxia Yang, Weidong Fei, Yu Zhao

Film preparation

A^{2+}-Zr^{4+} (A=Ca, Sr, Ba) co-doped $Bi_{(1-x)}A_xFe_{(1-x)}Zr_xO_3$ (x=0, 0.01, 0.02, 0.03, 0.04, 0.05) films were grown on Pt/Ti/SiO_2/Si substrates using Sol-Gel method. $Bi(NO_3)_3·5H_2O$ (99.99%), $Fe(NO_3)_3·9H_2O$ (99.99%), $Ca(NO_3)_2·4H_2O$ (99%), $C_4H_6O_4Sr$ (99%), $C_4H_6O_4Ba$ (99%) and $C_{12}H_{28}O_4Zr$ (70 wt. %) as the raw materials, ethylene glycol as the solvents, all drugs are purchased from Aladdin Reagent Company. First, 1.528 g $Bi(NO_3)_3·5H_2O$ (excessive 5%) and 1.212 g $Fe(NO_3)_3·9H_2O$ were dissolved in 10 mL ethylene glycol solution and heated at 60 °C for 3 h. After that, $Ca(NO_3)_2·4H_2O$/$C_4H_6O_4Sr$/$C_4H_6O_4Ba$ was dissolved in the solution cooled to room temperature, the $C_{12}H_{28}O_4Zr$ was added dropwise to the stirring solution to prevent aggregation. After that, the solution was continuously stirred for 2 h at room temperature after all solutes were dissolved, then the 0.3 mol/L precursor solutions were aged for 24 h. Second, Pt/Ti/SiO_2/Si substrates were immersed in hydrochloric acid, acetone and absolute ethanol for ultrasonic treatment (30 min). The residual anhydrous ethanol on the substrate surface was removed by high-purity argon gas, then the precursor solutions were

deposited on substrates through a multiple-step spin-coating procedure. The parameters of 2000 rpm for 10 s and then 8000 rpm for 30 s were used for a single spin-coating process, each wet layer was pyrolyzed on a hotplate at 350 ℃ for 10 min. Third, BFO films were heated in a rapid thermal annealing (RTA) equipment in air atmosphere. The entire heating stage is divided into five stages to avoid film rupture. Stage 1, 25~300 ℃ (30 s); Stage 2, 300~450 ℃ (30 s); Stage 3, 450~550 ℃ (20 s); Stage 4, 550~650 ℃ (20 s); Stage 5, 650 ℃ (300 s).

Film characterizations

The phase was characterized by X-ray diffraction (XRD) on a PANalytical B.V X-ray diffractometer experiment (Cu Kα radiation, λ= 1.5406 Å, 40 kV, 40 mA.) The step size and residence time of fine scan XRD are 0.02° and 5 s, respectively. The morphology and element distribution were observed by field emission scanning electron microscope (SEM, SU-5000, Hitachi). High-resolution transmission electron microscope (HRTEM) investigations were carried out on a Fei Talos F200x microscope. Focused ion beam (FIB, FEI LD Helios G5UX) technology was used to prepare the samples for TEM observations. The element valence was determined by a ThermoFisher Scientific X-Ray photoelectron spectroscopy (XPS, Al Kα =1486.6 eV, Esca Xi+).

Preparation method of gold electrodes

The top electrode of the thin film was fabricated using a magnetron sputtering system. A stainless steel mask with uniformly distributed 200 μm circular holes was placed on the film, and high-purity gold was selected as the sputtering target. The vacuum level during direct current magnetron sputtering was 1×10^{-5} Pa, and the sputtering pressure was 1 Pa. The operating voltage was set at 180 V, and the operating current was 0.04 A.

Photocurrent and temperature stability measurement

The photoelectric properties of the films were measured by an electrochemical workstation with two electrode system (Shanghai Chenhua Instrument Co., Ltd, China). 365 nm (10 mW/cm^2), 450 nm (150 mW/cm^2), 520 nm (150 mW/cm^2) and 400~800 nm (200 mW/cm^2) are light sources, the distance between the light source and film was maintained at 10 cm. For temperature stability measurement, the films were heated to the target temperature using an in-situ heating method, and each time the *J-V* curve was measured, it was obtained by cooling the film from the elevated temperature to room temperature. The following figure depicts the photovoltaic performance testing process of $BiFeO_3$ film.

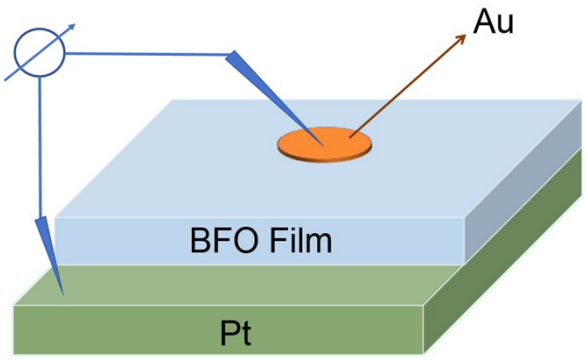

Schematic diagram of current voltage curve testing.

Reference:

1. H. Chen, W. Liu, Z. Qin, *Catal. Sci. Technol.* 7 (2017) 2236-2244.

2. S. M. Ahmed, P. Szymanski, L. M. El-Nadi, M. A. El-Sayed, *ACS Appl. Mater. Interfaces* 6 (2014) 1765-1772.

3. G. K. Mor, K. Shankar, M. Paulose, O. K. Varghese, C. A. Grimes, *Nano Lett*. 6 (2006), 215-218.

4. S. Y. Yang, J. Seidel, S. J. Byrnes, P. Shafer, C.-H. Yang, M. D. Rossell, P. Yu, Y.-H. Chu, J. F. Scott, J. W. Ager III, L. W. Martin, R. Ramesh, *Nature Nanotech*. 5 (2010) 143-147.

5. C. Lu, W. Hu, Y. Tian, T. Wu, *Appl*. *Phys*. *Rev*. 2 (2015) 021304.

6. Y. Zang, D. Xie, X. Wu, Y. Chen, Y. Lin, M. Li, H. Tian, X. Li, Z. Li, H. Zhu, T. Ren, D. Plant, *Appl*. *Phys*. *Lett*. 99 (2011) 132904.

7. J. Song, T. L. Kim, J. Lee, S. Y. Cho, J. Cha, S. Y. Jeong, H. An, W. S. Kim, Y. Jung, J. Park, G. Y. Jung, D. Kim, J. Y. Jo, S. D. Bu, H. W. Jang, S. Lee, *Nano Res*. 11 (2018) 642-655.

8. W. Dong, Y. Guo, B. Guo, H. Li, H. Liu, T. W. Joel, *ACS Appl. Mater. Interfaces* 5 (2013) 6925-6929.

9. C. Chen, W. Cai, M. Long, B. Zhou, Y. Wu, D. Wu, Y. Feng, *ACS Nano* 2010 4 6425-6432.

Fig. **S1** XRD analysis of BFO-CZ films, (a) XRD patterns, (b) (010) peaks and (c) (012)/(110) peaks with fine scanning of BFO-CZ.

Fig. **S2** XRD analysis of of BFO-SZ films, (a) XRD patterns, (b) (010) peaks and (c) (012)/(110) peaks with fine scanning.

Fig. **S3** XPS spectra of BFO-BZ films, (a) Bi 4f, (b) Fe 2p.

Fig. **S4** XPS spectra of O 1s in BFO-BZ films.

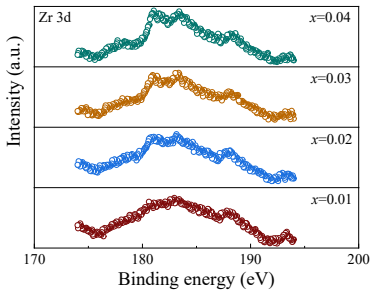

Fig. **S5** XPS spectra of Zr 3d in BFO-BZ films.

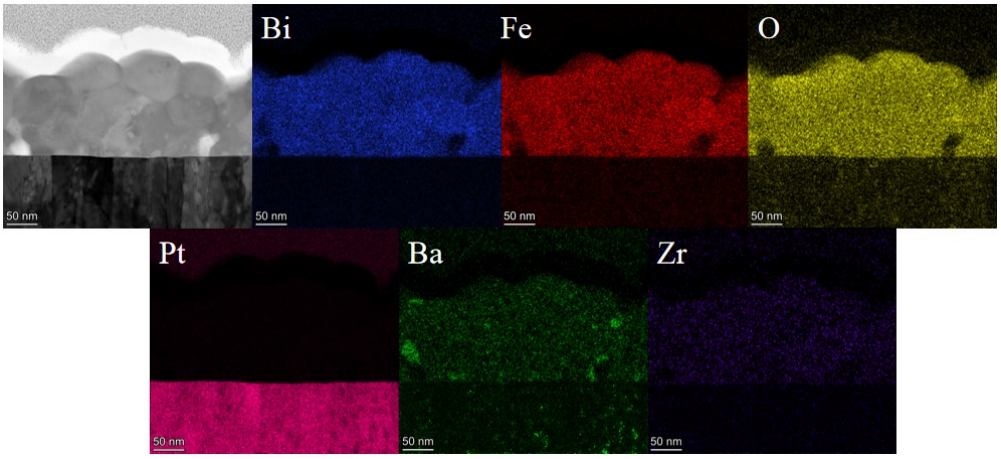

Fig. **S6** Cross sectional TEM images of BFO-0.03BZ and elemental mapping of Bi, Fe, O, Pt, Ba and Zr elements.

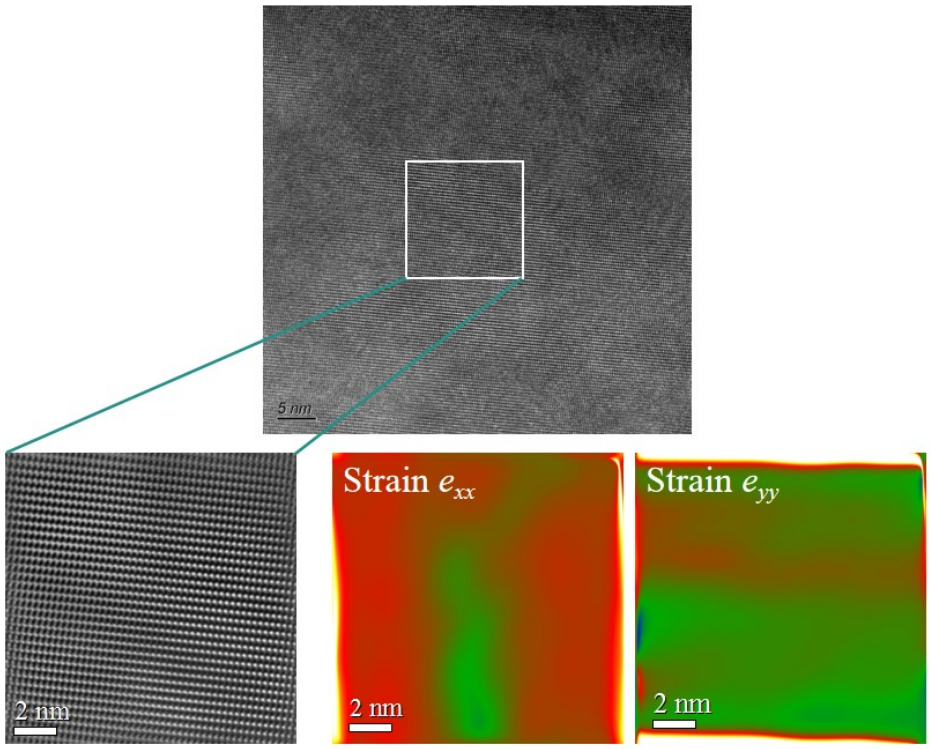

Fig. **S7** HRTEM image of the local lattice in pure BFO film, corresponding Fourier transform of the image in the white square, inverse FFT of the same region and in-plane strain tensor components e_{xx} and e_{yy} deduced by GPA.

Fig. **S8** *J-t* curves (zero bias, switchable) of BFO-CZ (a), BFO-SZ (b), and BFO-BZ (c) films under 450 nm (150 mW/cm^2) illumination.

Fig. **S9** *J-t* curves of BFO-CZ (a), BFO-SZ (b), BFO-BZ, and (c) films under 450 nm (150 mW/cm^2) long time illumination.

Fig. **S10** *J-V* curves, J_{SC} (left *y*-axis) and V_{OC} (right *y*-axis) curves with different doping content and *J-t* curves (zero bias, switchable) of BFO-CZ (a), BFO-SZ (b), and BFO-BZ (c) films under 365 nm (10 mW/cm^2) illumination.

Fig. **S11** *J-V* curves, J_{SC} (left *y*-axis) and V_{OC} (right *y*-axis) curves with different doping content and *J-t* curves (zero bias, switchable) of BFO-CZ (a), BFO-SZ (b), and BFO-BZ (c) films under 520 nm (160 mW/cm^2) illumination.

Fig. **S12** *J-V* curves, J_{SC} (left *y*-axis) and V_{OC} (right *y*-axis) curves with different doping content and *J-t* curves (zero bias, switchable) of BFO-CZ (a), BFO-SZ (b), and BFO-BZ (c) films under 400~800 nm (200 mW/cm^2) illumination.

Fig. **S13** *J-t* curves accompanied by the continuous switching of the light source for (a) BFO, (b) BFO-

CZ, (c) BFO-SZ, (d) BFO-BZ films.

Fig. **S14** *J-t* curves of BFO-CZ, BFO-SZ, BFO-BZ at treatments of 378 K (a) and 438 K (b) for different dime under 450 nm.